Nanoscale

ROYAL SOCIETY OF CHEMISTRY

PAPER

View Article Online
View Journal | View Issue

Check for updates

Cite this: *Nanoscale*, 2023, **15**, 6636

Photonic spin-selective perfect absorptance on planar metasurfaces driven by chiral quasi-bound states in the continuum

Hongju Li,[a] Hongmiao Zhou,[a] Gangao Wei,[a] Hangsheng Xu,[a] Meng Qin,*[a] Jianqiang Liu[b] and Feng Wu[c]

Received 4th January 2023,
Accepted 1st March 2023

DOI: 10.1039/d3nr00055a

rsc.li/nanoscale

Optical metasurfaces with high-quality-factor resonances and selective chirality simultaneously are desired for nanophotonics. Here, an all-dielectric planar chiral metasurface is theoretically proposed and numerically proved to support the astonishing symmetry-protected bound state in the continuum (BIC), due to the preserved π rotational symmetry around the z axis and up-down mirror symmetry simultaneously. Importantly, such BIC is a vortex polarization singularity enclosed by elliptical eigenstate polarizations with non-vanishing helicity, owing to the broken in-plane mirror symmetry. Under the oblique incidence, companied by the BIC transforming into a quasi-BIC (Q-BIC), the strong extrinsic chirality manifests. Assisted by the single-port critical coupling, the planar metasurface can selectively and near-perfectly absorb one circularly polarized light but non-resonantly reflect its counterparts. The circular dichroism (CD) approaching 0.812 is achieved. Intriguingly, the sign of CD (namely, the handedness of the chiral metasurface) can be flexibly manipulated only *via* varying the azimuthal angle of incident light, due to the periodic helicity sign flip in eigen polarizations around the BIC. Numerical results are consistent with the coupled-mode theory and multipole decomposition method. The spin-selective metasurface absorber empowered by the physics of chiral Q-BICs undoubtedly may promise various applications such as optical filters, polarization detectors, and chiral imaging.

Introduction

Symmetry is ubiquitous in the natural world. The symmetry in physics always describes the invariance of laws or geometries through a particular transformation pathway. Despite the beauty of symmetry, the study of symmetry breaking[1] has been important both scientifically and technologically in various areas. One such example is the chirality induced by complete breaking of mirror symmetry.[2] Chirality refers to an intrinsic property of a given object that cannot be brought to coincide with its mirror image by translation or rotation operator,[3,4] and is particularly important in pharmaceutics, biomedicine, and spectroscopy. The chiral phenomenon in optics is known as chiroptics,[5] which is originated from the interaction between circularly polarized light with different helicities and chiral objects. Chiroptics is manifested by a difference in amplitude, phase, and field distribution, when left- and right-circularly polarized light illuminate individually.[6] As a consequence, the new physical terms including optical activity,[7] circular birefringence,[8] and circular dichroism (CD),[9] have been proposed to characterize the distinguishable chiroptical responses. Chiral optical absorption, as an enduring branch of chiral light–matter interaction,[10–12] has found significant applications in polarization imaging, photodetection, filtering, and many other fields. Chiral absorption in natural materials is extremely weak, due to the small size of molecular structure relative to the wavelength of incident light.[13,14] The structures with geometric chiral properties on length scales comparable with the wavelength of incident light are desired to realize strong chiroptical absorption.[15] Artificial metamaterials[16,17] with unit cells on sub-wavelength scale that is typically much larger than the size of molecular naturally have received burgeoning amount of interest recently. Benefiting from the flexible structure design and strong near-field enhancement, various metal-based chiral metamaterial absorbers have been successively proposed by breaking the mirror symmetry in the propagation direction.[18] Examples include the double-layered L-shaped copper antennas,[19] bi-layered fourfold twisted T-shaped structure,[20] four rotated twisted closed ring resonators,[21] and so on. Beyond the three-dimensional

---

[a] *School of Physics, Hefei University of Technology, Hefei, Anhui 230009, China. E-mail: qinm@hfut.edu.cn*

[b] *School of Science, Jiujiang University, Jiujiang 332005, China*

[c] *School of Optoelectronic Engineering, Guangdong Polytechnic Normal University, Guangzhou 510665, China*

metamaterials,[22,23] the two-dimensional counterparts (which are also referred as metasurfaces[24–27]) with broken in-plane mirror symmetry are capturing interest, because they do not require very demanding nanofabrication techniques. Examples include the double-rectangle gold bars,[28,29] η-shaped silver resonators,[30] Z-shaped silver antennas,[31] and other planar chiral structures.[32] Although the metal-based chiral metamaterials can near-perfectly absorb one circularly polarized light but non-resonantly reflect its counterparts, the quality factor (*Q*-factor) of absorption peaks and the extremum of CD are limited by the inevitable Ohmic loss and heating problem in metals.[33] Importantly, once the metamaterial with a specific shape is fabricated, its handedness and the sign of CD are irrevocable.[6] Hence, the realization of chiral metasurface absorbers with high *Q*-factor and tunable spin selectivity simultaneously is urgent.

The symmetry-protected bound states in the continuum (BICs)[34–38] on all-dielectric planar metasurfaces, to the best of our knowledge, may provide a feasible way to achieve such desired chiral absorbers. On the one hand, the BICs are identified as non-radiating eigenvalues of electromagnetic wave equation above the light cone.[39] The nearly real eigenfrequency mode,[40] characterized by an unbounded *Q*-factor and vanishing linewidth, indicates that the ideal BICs will be invisible in absorptance spectra and cannot be externally accessed.[41] Fortunately, the small perturbation from breaking in the mirror symmetry of metasurfaces not only enables the symmetry-protected BICs to be transformed into externally accessible quasi-BICs (Q-BICs)[42–47] with ultrahigh *Q*-factors but also may give rise to the chiral response.[48–52] On the other hand, the BICs have been proved to be vortex centers in the polarization directions of far-field radiation.[53] The winding structure of polarization states in the momentum space offers a new avenue to modulating polarization. Especially, due to the appearance of circularly polarized states induced by in-plane symmetry breaking, modulating the handedness of a chiral metasurface supporting the original symmetry-protected BICs is possible.[54–56] Therefore, the planar metasurface supporting a symmetry-protected BIC enclosed by elliptical eigenstate polarizations with non-vanishing helicity in momentum space is an ideal candidate to obtain chiral absorbers with ultrahigh *Q*-factors and actively tunable spin selectivity simultaneously.

Here, two pairs of parallel and staggered silicon bars are orthogonally placed to form a planar metasurface. The preserved π rotational symmetry around the *z* axis (C_2^z) and simultaneously the up-down mirror symmetry along the *z* direction (σ_z) ensure the metasurface to support the fantastic symmetry-protected BIC. The additional breaking in the in-plane mirror symmetry leads to that the vortex polarization singularity at the BIC is enclosed by elliptical eigenstate polarizations with non-vanishing helicity. Under the oblique incidence, not only is the symmetry-protected BIC transformed into a Q-BIC with high *Q*-factor but also the strong extrinsic chirality emerges. Assisted by the single-port critical coupling, this planar metasurface thus can near-perfectly absorb one circularly polarized light but non-resonantly reflect its counterparts. Accompanied by the realization of chiral absorption, the CD approaching 0.812 is observed. Intriguingly, the sign of CD (namely, the handedness of the chiral metasurface) can be actively manipulated only *via* varying the azimuthal angle of incident light, due to the periodic helicity sign flip in eigen polarizations around the Γ point at the first Brillouin zone. Numerical results are in excellent agreement with the coupled-mode theory (CMT) and multipole decomposition method. The spin-selective metasurface perfect absorber empowered by the physics of BICs undoubtedly may find utility in optical filters, polarization detectors, and imaging display.

Structure and principle

Fig. 1 shows the schematic illustration of the designed chiral metasurface on a metallic substrate. The unit cell comprises two pairs of parallel and staggered rectangular silicon bars, which are orthogonally placed and intersect at the origin, as displayed in Fig. 1(b). The schematic drawing of unit cell with detailed geometry definitions is shown in Fig. 1(a). The width and length of two identical rectangular silicon bars along *x* axis are denoted by W_1 and L_1, respectively. Similarly, the width and length of the silicon bars along *y* axis are marked by W_2 and L_2, respectively. The thickness of all silicon bars is *H*. The period of the fabricated silicon metasurface arranging in a square lattice is *a*, and the thickness of metallic substrates is *D*. To simplify the absorption mechanism, the metallic substrate with thickness of $D = 400$ nm is considered. This thickness is much larger than the penetration depth of electromagnetic waves so that the investigated structure is degraded into a single-port system without the transmission channel. Certainly, in addition to the ultra-thickness metallic substrate, an all-dielectric Bragg mirror can enable this structure to work as a single-port system in principle. Such simple single-port

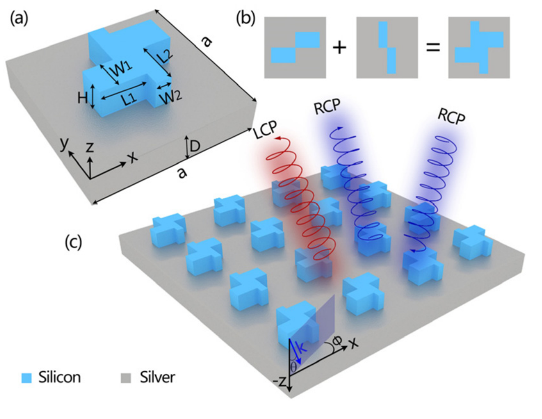

Fig. 1 Schematic illustration of the designed chiral metasurface on a silver substrate. (a) Geometry of the unit cell. (b) The top view of the unit cell. (c) Illustration of the periodic planar metasurface illuminated by circularly polarized light with the incident angle *θ* relative to *z* axis and the azimuthal angle *Φ* relative to *x* axis.

system permits the use of critical coupling to obtain the potential perfect absorption.[57–59]

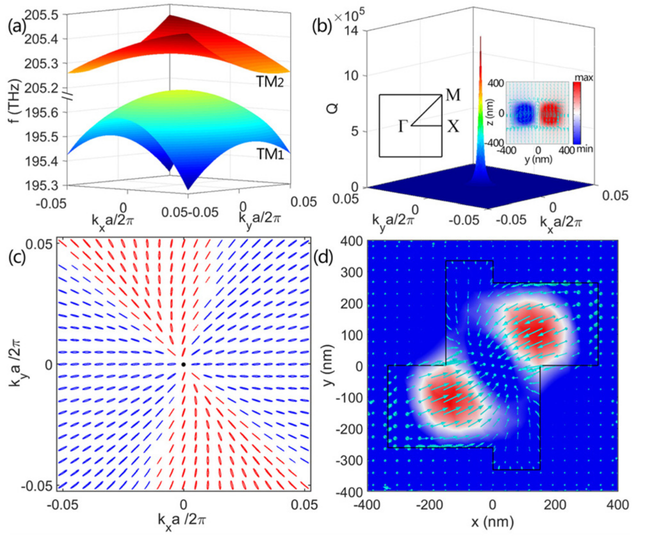

Fig. 2 The eigenmode analysis of the isolated periodic chiral metasurface. (a) The simulated transverse magnetic (TM) band structures. (b) The calculated Q-factors of the TM_1 band. The radiative Q-factor diverges at the Γ point, indicating the occurrence of a symmetry-protected BIC. The left inset denotes the schematic of first Brillouin zone of a square lattice. The right inset shows the magnetic field (H_x) distributions on the x = 0 nm slice for the symmetry-protected BIC. The arrows indicate the electric field vector. (c) The eigen polarization map at the first Brillouin zone for the TM_1 band. The polarization states are represented by ellipses. The red and blue colors correspond to the left-handed and right-handed states, respectively. The black dot denotes a vortex polarization singularity, known as the unique BIC. (d) The magnetic field distributions at the plane of z = 0 nm for the symmetry-protected BIC. Overlaid on the colour map is the plot of the electric field vector denoted by the light blue arrows.

Firstly, the eigenmodes of an isolated periodic metasurface made from lossless silicon with a refractive index of n = 3.478 are numerically analyzed by using the finite element method. The optimized geometric parameters are H = 360 nm, W_1 = 260 nm, W_2 = 148 nm, $L_1 = L_2$ = 330 nm, and a = 800 nm. The $W_1 \neq W_2 \neq L_1$ indicates that the metasurface maintains the $C_2^{\,z}$ symmetry and σ_z symmetry simultaneously, but suffers from the loss of in-plane mirror symmetry. In theory, the combination of $C_2^{\,z}$ symmetry and the σ_z symmetry is the sufficient condition for a stable symmetry-protected BIC.[53] In the implementation, the eigenfrequency solver in COMSOL Multiphysics software is utilized to calculate the eigenmodes. The Floquet periodic boundary conditions are applied in the x and y directions to determine the in-plane wavevectors (k_x, k_y), and the perfectly matched layers are used in the z direction to absorb the radiation wave. Here, we restrict the discussion to transverse-magnetic-like eigenmodes as they have much higher Q-factors than transverse-electric-like modes in the wavelength range of interest. To select the transverse magnetic (TM) eigenstates, a perfect electric conductor as boundary condition is set at the middle of the metasurface. Two TM band structures with real parts of eigenfrequencies in the first Brillouin zone are shown in Fig. 2(a). The first Brillouin zone of a square lattice is schematically shown in the left inset of Fig. 2(b). Comparison of two TM band structures exhibits that the TM_1 mode with a relatively flat band at the Γ point has smaller imaginary parts of complex eigenfrequencies expressed by $f = f_0 + \mathrm{j}\eta$, in which the real part f_0 is the resonance frequency and the imaginary part η represents the leakage rate. In other words, the TM_1 eigenmode possesses higher Q-factor, which is defined as $Q = \frac{1}{2}\frac{\mathrm{Re}(f)}{\mathrm{Im}(f)} = \frac{f_0}{2\eta}$. The calculated Q-factors for the TM_1 band at the first Brillouin zone are shown in Fig. 2(b). It is interesting to note that the radiative Q-factor diverges at the Γ point, indicating the occurrence of a symmetry-protected BIC (also referred as the Γ-state BIC).[36]

Another hard evidence for a symmetry-protected BIC is that the vortex polarization singularity occurs at the Γ point in the eigen polarization map of the TM_1 band, as indicated by the black dot in Fig. 2(c). The magnetic field profiles of the BIC at different slices are shown in the Fig. 2(d) and the right inset of Fig. 2(b), respectively. Combination of mode profiles indicates that the BIC can be treated as a pair of anti-parallel magnetic dipoles along the x axis. Assisted by the C_2 group symmetry analysis,[60,61] we can further understand the perfectly confined BIC. As shown in Fig. 2(d), the magnetic field of the BIC at the Γ point is even under the π rotation around the incident direction (the z axis). However, for Γ point of the reciprocal space, the one and only radiation channel for the sub diffractive regime is the plane wave propagating along the z axis, and its electromagnetic fields, meanwhile, should be odd under the same $C_2^{\,z}$ operator. Due to the symmetry mismatch between the mode profile inside the metasurface and that of the external propagating wave, the TM_1 eigenmode cannot be excited by any linearly polarized plane waves under normal incidence, and thus behaves as a typical symmetry-protected BIC that cannot be accessed externally.

Another striking feature in Fig. 2(d) is that the field profile has a spatial inversion symmetry, which will allow the local response to be birefringent.[49] In combination with the lack of any in-plane mirror symmetry, the metasurface will manifest the inherent planar chirality,[62–64] and the intrinsic BIC thus is enclosed by vortex elliptical eigen polarizations with non-vanishing helicity, as already shown in Fig. 2(c). The helicity sign periodically flips around the Γ point. The opposite helicity of eigen polarizations along the x and y directions is observed. Under the oblique incidence of circularly polarized light, the symmetry-protected BIC will be transformed into a chiral Q-BIC with high Q-factor. The planar metasurface thus manifests the strong extrinsic chirality. More importantly, the periodic helicity sign flip of the Q-BIC around the Γ point in the momentum space will promise a feasible way of only by changing the azimuthal angle of circularly polarized light under oblique incidence to actively modulate the handedness of the chiral metasurface, as indicated in Fig. 1(c).

Simulation and discussion

To verify the potential spin-dependent optical response of the chiral metasurface driven by the physics of BIC, the chiral absorber enabled by the single-port system is comprehensively investigated. The metallic substrate is assumed to be silver whose relative permittivity is characterized by the typical Drude model $\varepsilon_\mathrm{m}(\omega) = \varepsilon_\infty - \omega_\mathrm{p}{}^2/(\omega^2 + \mathrm{j}\omega\gamma)$.[65–67] Here, we consider the $\varepsilon_\infty = 3.7$, $\omega_\mathrm{p} = 9.1$ eV, and $\gamma = 0.018$ eV at the near-infrared region. Other parameters are same as those used for Fig. 2. Without the transmission, the Jones matrix of reflection coefficient (r) under circular polarization basis is enough for illustrating the chiral absorption response.[68]

$$J_{circ} = \begin{pmatrix} r_{rr} & r_{rl} \\ r_{lr} & r_{ll} \end{pmatrix}. \tag{1}$$

Here, the subscripts r and l represent the right-handed polarization (RCP) and left-handed polarization (LCP), respectively. The r_{ij} ($i = r, l$ and $j = r, l$) stands for the reflection coefficient of output polarization i from input polarization j. The absorptance of the incident LCP and RCP lights can be respectively expressed as

$$\begin{aligned} A_{LCP} &= 1 - |r_{ll}|^2 - |r_{rl}|^2 = 1 - R_{ll} - R_{rl}, \\ A_{RCP} &= 1 - |r_{rr}|^2 - |r_{lr}|^2 = 1 - R_{rr} - R_{lr}. \end{aligned} \tag{2}$$

The $R_{ij} = |r_{ij}|^2$ is the reflection of the system. Additionally, to highlight the chirality of the metasurface, the CD is defined as the reflection difference and is described as[49]

$$CD = \frac{(R_{rr} + R_{lr}) - (R_{ll} + R_{rl})}{(R_{rr} + R_{lr}) + (R_{ll} + R_{rl})}. \tag{3}$$

The evolution of simulated reflection spectra of all Jones matrix elements by continuously varying incident angle θ along the x direction ($\Phi = 0°$) is shown in Fig. 3. We note that all incident lights are totally reflected at the normal incidence ($\theta = 0°$), indicating that there is no resonant mode excited on the metasurface in this case. Under the oblique incidence, however, an obvious dip appears at the co-polarized reflection spectra (R_{ll} and R_{rr}), as shown in Fig. 3(a) and (c), respectively. Meanwhile, as the $|\theta|$ increases, the reflection dip gradually drops with expanded linewidth and its resonant wavelength experiences a redshift. Such observation is the direct evidence for the transformation of an unobservable BIC to the accessible Q-BIC. Notably, in addition to the nearly same reflection spectra for the co-polarized R_{ll} and R_{rr}, the striking difference in the cross-polarized reflection spectra (R_{rl} and R_{lr}) is observed in Fig. 3(b) and (d). Based on the eqn (2), the chiral absorption will be achieved on the metasurface under the oblique incidence. The calculated absorptance spectra as a function of θ are shown in Fig. 4. Comparison of Fig. 4(a) and (b) suggests that companied by the appearance of chiral Q-BIC resonance under the oblique incidence, the metasurface indeed can strongly absorb left-circularly polarized (LCP) light, whereas non-resonantly reflect the right-circularly polarized (RCP) light. As excepted, with the $|\theta|$ increasing, the absorptance peak of LCP light gradually arises with expanded linewidth and its spectral position tends to exhibit a redshift simultaneously. The calculated CD spectra are shown Fig. 4(c). The CD as high as 0.812 is observed. Therefore, the strong external chirality empowered by the Q-BIC resonance on the planar metasurface is achieved.

Fig. 4(d) and (e) demonstrate the absorptance spectra as a function of incident angle θ varying along the y direction (Φ =

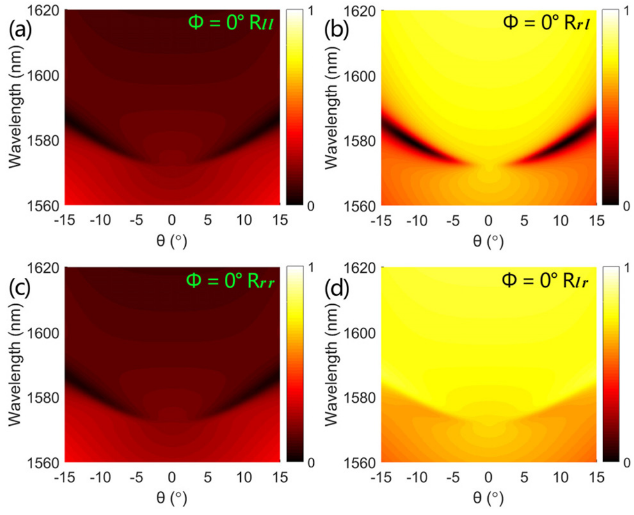

Fig. 3 The evolution of reflection spectra of all Jones matrix elements on the incident angle θ that varies along the x axis (*i.e.*, the azimuthal angle is $\Phi = 0°$). (a)–(d) correspond to the Jones matrix elements of R_{ll}, R_{rl}, R_{rr}, and R_{lr}, respectively.

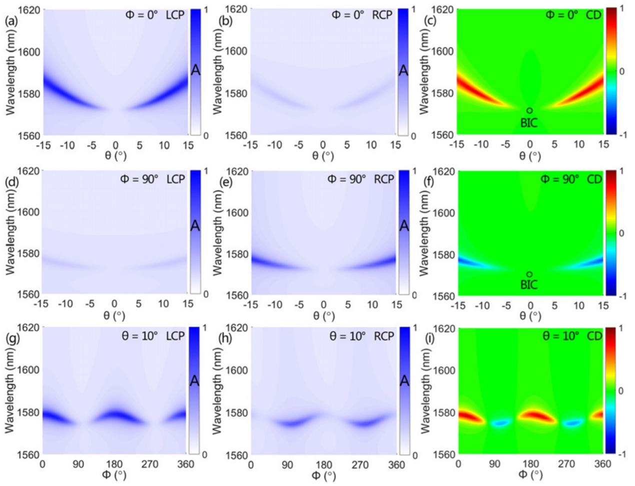

Fig. 4 Absorptance and CD spectra of the chiral metasurface. Absorptance spectra with respect to the incident angle θ for (a) LCP and (b) RCP illuminations with a fixed azimuthal angle of $\Phi = 0°$. (c) CD spectra with respect to the θ varying along the x direction ($\Phi = 0°$). Absorptance spectra as a function of θ for (d) LCP and (e) RCP illuminations with a fixed azimuthal angle of $\Phi = 90°$. (f) CD spectra with respect to the θ varying along the y direction ($\Phi = 90°$). Absorptance spectra as a function of the azimuthal angle Φ for (g) LCP and (h) RCP illuminations with a fixed incident angle of $\theta = 10°$. (i) CD spectra as a function of the azimuthal angle Φ with a fixed incident angle of $\theta = 10°$.

90°). In stark contrast to the results in Fig. 4(a) and (b), the metasurface strongly absorbs RCP light and non-resonantly reflects the LCP light, when the incident angle varies along the y direction ($\Phi = 90°$). Compared to the Fig. 4(c), as a result, the sign flip of CD is observed in the Fig. 4(f). The combination of Fig. 4(c) and (f) suggests that the planar metasurface driven by the chiral Q-BIC resonance can exhibit opposite handedness only by varying the incident angle along x and y directions, respectively. Such superior spin selectivity can be attributed to the opposite helicity of eigen polarizations along the k_x and k_y directions, as shown in Fig. 2(c). Therefore, we can selectively modulate the handedness of the chiral metasurface by changing the azimuthal angle of the incident light, according to the helicity of eigen polarizations around the Γ point at the first Brillouin zone. The absorptance and CD spectra as a function of the azimuthal angle Φ are presented in Fig. 4(g)–(i). The incident angle is fixed at $\theta = 10°$ to observably excite the Q-BIC resonance. As expected, the azimuthal angle of incident light indeed behaves as a key factor to switch the handedness of the chiral metasurface. As the Φ evolves from 0 to 360°, the opposite varying trend is observed at the absorptance spectra of LCP and RCP light, as shown in Fig. 4(g) and (h), respectively. The periodic sign flip of CD thus is achieved with the increase of Φ, as shown in Fig. 4(i). The observation in Fig. 4(i) matches well with the helicity sign flip of the eigen polarizations around the Γ point in Fig. 2(c). Empowered by the abundant physics of BIC on the planar metasurface, hence, we not only realize a chiral absorber but also can actively manipulate its handedness only through handily varying the azimuthal angle of the incident light, unlike the conventional ways where fabricating a new structure would be essential for switching the handedness.

We also confirm the chiral Q-BIC on the metasurface by the multipole decomposition method.[69–72] The five leading multipole moments including electric dipole (ED) moment $\left(\vec{P}\right)$, magnetic dipole (MD) moment $\left(\vec{M}\right)$, toroidal dipole (TD) moment $\left(\vec{T}\right)$, electric quadrupole (EQ) moment $\left(Q_{\alpha\beta}^{(e)}\right)$, and magnetic quadrupole (MQ) moment $\left(Q_{\alpha\beta}^{(m)}\right)$ are calculated by using the expressions.[69]

$$\vec{P}=\frac{1}{i\omega}\int\vec{J}\,d^3r, \tag{4}$$

$$\vec{M}=\frac{1}{2c}\int\left(\vec{r}\times\vec{J}\right)d^3r, \tag{5}$$

$$\vec{T}=\frac{1}{10c}\int\left[\left(\vec{r}\cdot\vec{J}\right)\vec{r}-2r^2\vec{J}\right]d^3r, \tag{6}$$

$$\left.\begin{aligned}Q_{\alpha\beta}^{(e)}&=\frac{1}{i\omega}\int\left[r_\alpha J_\beta+r_\beta J_\alpha-\frac{2}{3}\left(\vec{r}\cdot\vec{J}\right)\right]d^3r\\ Q_{\alpha\beta}^{(m)}&=\frac{1}{3c}\int\left[\left(\vec{r}\times\vec{J}\right)_\alpha r_\beta+\left(\vec{r}\times\vec{J}\right)_\beta r_\alpha\right]d^3r\end{aligned}\right\}\quad\alpha,\beta=x,y,z. \tag{7}$$

Here, c is the speed of light in vacuum and ω is its angular frequency. The $\vec{r}$ is the distance vector from the origin to point (x, y, z) in the Cartesian coordinate. The $\vec{J}$ is the displacement current density within a unit cell of the chiral silicon metasurface. The far-field scattered energy from multipole excitation is respectively calculated by[72]

$$\begin{aligned}&I_P=\frac{2\omega^4}{3c^3}\left|\vec{P}\right|^2,\ I_M=\frac{2\omega^4}{3c^3}\left|\vec{M}\right|^2,\ I_T=\frac{2\omega^6}{3c^5}\left|\vec{T}\right|^2,\\ &I_{Q^{(e)}}=\frac{\omega^6}{5c^5}\sum\left|Q_{\alpha\beta}^{(e)}\right|^2,\ I_{Q^{(m)}}=\frac{\omega^6}{20c^5}\sum\left|Q_{\alpha\beta}^{(m)}\right|^2.\end{aligned} \tag{8}$$

Without loss of generality, the oblique incidence with $\theta = 10°$ and $\Phi = 0°$ as an example is considered. As already shown in Fig. 4(a), under the illumination of LCP light, the Q-BIC resonance is excited at $\theta = 10°$ and the nearly perfect absorptance peak is observed at the wavelength of 1581 nm. On the contrary, without the excitation of the Q-BIC resonance on the metasurface, the incident RCP light is almost completely reflected, as shown Fig. 4(b). Scattered powers of five leading multipoles on the chiral metasurface under LCP and RCP illumination are demonstrated in Fig. 5(a) and (b), respectively. For the illumination of LCP light with $\theta = 10°$ and $\Phi = 0°$, the excited Q-BIC resonance primarily dominated by the MD is observed in Fig. 5(a), which is consistent with the result from

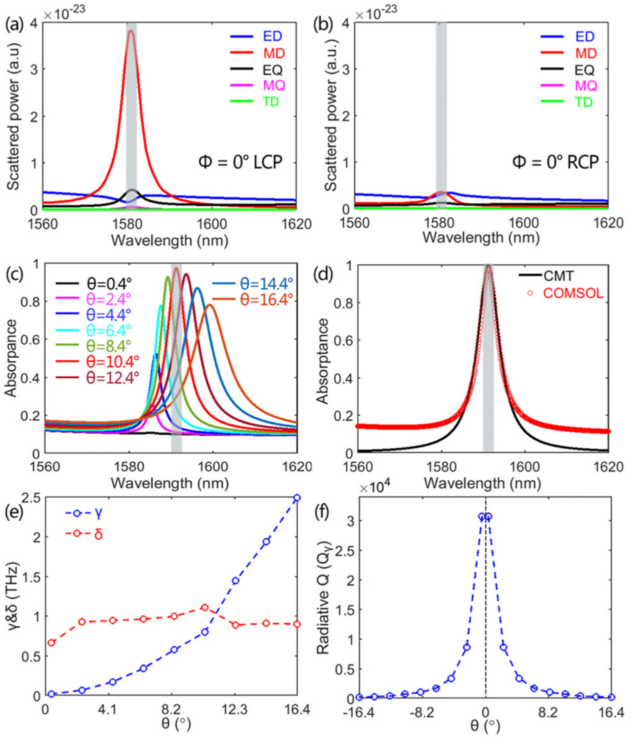

Fig. 5 Scattered energy of five leading multipoles of the chiral metasurface under LCP (a) and RCP (b) illumination with $\theta = 10°$ and $\Phi = 0°$. (c) The evolution of absorptance spectra of LCP light on the incident angle varying from 0.4° to 16.4° in intervals of 2° along the x direction ($\Phi = 0°$). The other parameters are same as those used in Fig. 2, except for the a = 846 nm. (d) The CMT-fitted and numerically simulated absorptance spectra at critical coupling of $\theta = 10.4°$. (e) The calculated radiative loss rate γ and dissipative loss rate δ for different θ. (f) The calculated radiative Q-factor (Q_γ) for different θ.

the eigenmode analysis in Fig. 2 where the BIC is characterized by a pair of anti-parallel magnetic dipoles along the x axis. For the illumination of RCP light in Fig. 5(b), however, the contributions from the multipoles are suppressed at the wavelength of 1581 nm, and thus the excitation of a Q-BIC resonance is prohibited. Therefore, the extrinsic chiral response of the metasurface is again verified to be attributed to the chiral Q-BIC resonance, which is primarily dominated by the MD and is only excited by one circularly polarized light at a time.

In addition, it is well known that the radiative Q-factor of the Q-BIC resonance gradually decreases as the incident angle increases, due to the expanded leakage channel. Therefore, the linewidth of the absorptance peak enabled by the Q-BIC expands gradually with the incident angle increasing, as already shown in Fig. 4(a). Particularly, we observe that the absorptance intensity increases at the beginning and then decreases as the incident angle increases, according to the enlarged absorptance spectra in Fig. 5(c). In the Fig. 5(c), the absorptance spectra for the incident angle increasing from 0.4° to 16.4° in intervals of 2° are demonstrated. The absorptance intensity increases as the θ increases from 0.4° to 10.4°, and reaches a maximum at $\theta = 10.4°$. The further increase in the θ, however, leads to the decrease of absorptance intensity. The proposed single-port system permits the use of the versatile CMT[73–75] to reveal the unusual behavior in the absorptance intensity induced by the change in θ.

When the intrinsic Q-BIC is excited by the LCP light under the oblique incidence of $\Phi = 0°$, the dynamic equations for the single-port system are described by[74]

$$\frac{\mathrm{d}a_{\mathrm{Q-BIC}}}{\mathrm{d}t} = (\mathrm{j}\omega_0 - \gamma - \delta)a_{\mathrm{Q-BIC}} + \mathrm{j}\sqrt{2\gamma}S_+, \tag{9}$$

$$S_- = -S_+ - \mathrm{j}\sqrt{2\gamma}a_{\mathrm{Q-BIC}}. \tag{10}$$

Here, $a_{\text{Q-BIC}}$ and ω_0 denote the amplitude and frequency of the Q-BIC, respectively. The j stands for the imaginary unit. The γ and δ represent the radiative loss rate and dissipative loss rate of the Q-BIC, respectively. The S_+ and S_- stand for the amplitudes of input and output waves, respectively. Using the general frequency domain $e^{+\mathrm{j}\omega t}$ to isolate the S_-/S_+, the reflection coefficient of the system is expressed as

$$r_{\text{total}} = \frac{S_-}{S_+} = -\frac{\mathrm{j}(\omega - \omega_0) + \delta - \gamma}{\mathrm{j}(\omega - \omega_0) + \gamma + \delta}. \tag{11}$$

The absorptance of the system is obtained by $A_{\text{LCP}} = 1 - |r_{\text{total}}|^2$ and thus is expressed as

$$A_{\text{LCP}} = 1 - |r_{\text{total}}|^2 = 1 - R_{\text{total}} = \frac{4\delta\gamma}{(\omega - \omega_0)^2 + (\gamma + \delta)^2}. \tag{12}$$

The eqn (12) shows that the maximum absorptance at the resonant frequency of ω_0 is determined by the γ and δ. It is expressed as

$$A_{\omega_0} = \frac{4\delta\gamma}{(\gamma + \delta)^2}. \tag{13}$$

The half-maximum absorptance at the resonant frequency ω_1 is

$$A_{\omega_1} = \frac{4\delta\gamma}{(\omega_1 - \omega_0)^2 + (\gamma + \delta)^2}. \tag{14}$$

Because of the $A_{\omega_0} = 2A_{\omega_1}$, the full width at half maximum (Γ) is obtained by

$$\Gamma = 2|\omega_1 - \omega_0| = 2(\gamma + \delta). \tag{15}$$

The total Q-factor of the absorptance peak is defined by

$$Q_{\text{total}} = \frac{\omega_0}{\Gamma} = \frac{\omega_0}{2|\omega_1 - \omega_0|} = \frac{\omega_0}{2(\gamma + \delta)} \tag{16}$$

Similarly, the radiative and dissipative Q-factors can be respectively calculated by

$$Q_\gamma = \frac{\omega_0}{2\gamma}, \quad Q_\delta = \frac{\omega_0}{2\delta}. \tag{17}$$

The eqn (13) shows that the realization of perfect absorptance at the resonant frequency of ω_0 is possible, when the $\gamma = \delta$ occurs. The $\gamma = \delta$ suggests that the energy is coupled into the system at the same rate as that of the dissipation, and thus is defined as the critical coupling.[74] Besides the critical coupling, the $\gamma < \delta$ is defined as the under coupling, whereas the $\gamma > \delta$ is defined as the over coupling. At the under coupling of $\gamma < \delta$, the reflection coefficient at the resonant frequency ω_0 is expressed as

$$r_{\text{total}}^{\omega_0} = \sqrt{R_{\text{total}}^{\omega_0}} = -\frac{\gamma - \delta}{\gamma + \delta}. \tag{18}$$

In combination with the eqn (16) and (17), we can obtain the radiative Q-factor (Q_γ) and dissipative Q-factor (Q_δ).

$$\begin{cases} Q_\gamma = \dfrac{2Q_{\text{total}}}{1 - \sqrt{R_{\text{total}}^{\omega_0}}} \\ Q_\delta = \dfrac{2Q_{\text{total}}}{1 + \sqrt{R_{\text{total}}^{\omega_0}}} \end{cases}. \tag{19}$$

At the over coupling of $\gamma > \delta$, the reflection coefficient at the resonant frequency ω_0 is expressed as

$$r_{\text{total}}^{\omega_0} = \sqrt{R_{\text{total}}^{\omega_0}} = \frac{\gamma - \delta}{\gamma + \delta}. \tag{20}$$

The Q_γ and Q_δ are expressed as

$$\begin{cases} Q_\gamma = \dfrac{2Q_{\text{total}}}{1 + \sqrt{R_{\text{total}}^{\omega_0}}} \\ Q_\delta = \dfrac{2Q_{\text{total}}}{1 - \sqrt{R_{\text{total}}^{\omega_0}}} \end{cases}. \tag{21}$$

The calculated radiative loss rate γ and dissipative loss rate δ for different incident angles are shown in Fig. 5(e). They are extracted from the absorptance spectra in Fig. 5(c) by using the eqn (16)–(21). Considering the BIC-driven chiral metasurface absorber, the radiative channel of the symmetry-protected BIC opens under the oblique incidence, and thus, the ideal BIC is turned into a leaky resonance (Q-BIC). With the incident angle increasing, the radiative loss rate γ of the Q-BIC increases from zero to finite values, as indicated by the blue curve in Fig. 5(e). However, the dissipative loss of the Q-BIC is ascribed to the neighboring metallic substrate, because the silicon metasurface is treated as lossless. Thus, the dissipative loss rate δ is considered to nearly remain unchanged as the incident angle increases, as demonstrated by the red curve in Fig. 5(e). Interestingly, with the incident angle increasing, the crossing between γ and σ appears at $\theta = 10.4°$, indicating the occurrence of critical coupling. Therefore, the system successively experiences the under coupling, critical coupling, and over coupling, as the θ varies from 0.4° to 16.4°. As expected, we observe that the absorptance intensity increases as the θ increases from 0.4° to 10.4° and reaches a maximum at $\theta = 10.4°$ in Fig. 5(c). When the θ further increases, the system drops into the over coupling region and the perfect absorptance is destructed. The simulated result is in excellent agreement with that obtained by the CMT. As a specific example, the nearly perfect absorptance at the critical coupling is fitted very well by the CMT in the Fig. 5(d). We also show the calculated radiative Q-factor as a function of incident angle in Fig. 5(f). As a characteristic feature of an ideal symmetry-protected BIC,[34] the inverse quadratic law between Q_γ and the asymmetric parameter θ is observed.

So far, assisted by the physics of chiral Q-BIC and the single-port critical coupling, the chiral perfect absorber with tunable spin selectivity is successfully realized. The established planar microfabrication techniques,[76–78] such as the electron beam lithography companied by the processes of deposition, patterning, lift-off, and etching, are competent for the construction of such planar silicon metasurface. The robustness of the chiral perfect absorptance is also investigated *via* changing the structural parameters including W_1, L_1, H, and a. The chiral metasurface under LCP illumination with $\theta = 10°$ and $\Phi = 0°$ as an example is considered. The nearly perfect absorption spectrum is obtained, as shown in Fig. 4(a). Fig. 6(a)–(d) show the evolution of absorptance spectra on the W_1, L_1, H, and a, respectively. Because the chiral response is empowered by the Q-BIC resonance evolved from an ideal symmetry-protected BIC, the chiral absorptance will remain unchanged as long as the $C_2{}^z$ symmetry and σ_z symmetry are preserved by the metasurface. Additionally, the Q-BIC resonance is characterized by a pair of anti-parallel magnetic dipoles along the x axis, and its field is mainly confined in the two silicon bars arranging in the x direction, as shown in Fig. 2(d). The circular electric field within the y–z cross section of silicon bars arranging in the x direction is also observed in the right inset of Fig. 2(b). Therefore, at a fixed incident angle, the wavelength of the Q-BIC resonance will be determined by the width W_1 and height H of the silicon bars arranging in the x direction. The changes in other structural parameters including a, L_1, and W_2, will have little effect on the resonant wavelength of the Q-BIC. Simulated results confirm the qualitative analysis mentioned above. As shown in Fig. 6(a) and (c), the spectral position of the absorptance peak indeed tends to exhibit a redshift with the width W_1 and height H increasing, respectively. The expected robustness of absorptance spectra with the L_1 and a individually varying is also witnessed in Fig. 6(b) and (d), respectively.

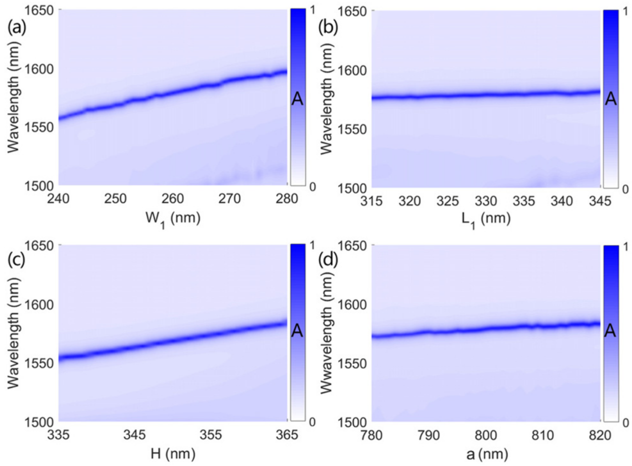

Fig. 6 The dependence of absorptance spectra on structural parameters. Absorptance spectra as a function of W_1 (a), L_1 (b), H (c), and a (d), respectively. Other simulated details are identical to those used in Fig. 5(a), except the variable parameter in each subfigure.

Conclusions

In summary, we have both theoretically and numerically investigated the photonic spin-selective absorptance on a planar metasurface enabled by the chiral Q-BIC. The total absorptance of one circularly polarized light but non-resonantly reflection of its counterparts is realized. The CD up to 0.812 is observed. Intriguingly, the spin selectivity of the chiral metasurface and the corresponding sign of CD can be handily modulated only *via* varying the azimuthal angle of the incident light, instead of fabricating a new structure. All numerical observes are consistent with those obtained by the CMT and multipole decomposition method. The robustness of the chiral perfect absorptance under the changes in the structural parameters is also comprehensively demonstrated. The chiral metasurface perfect absorber with actively tunable handedness undoubtedly may find utility in optical filters, polarization detectors, and imaging display.

Author contributions

Hongju Li: conceptualization, software, data curation, formal analysis, investigation, methodology, writing – original draft, funding acquisition. Hongmiao Zhou: writing – review and editing. Gangao Wei: writing – review and editing. Hangsheng Xu: writing – review and editing. Meng Qin: writing – review and editing, supervision, funding acquisition. Jianqiang Liu: software, writing – review and editing. Feng Wu: writing – review and editing, funding acquisition.

Conflicts of interest

There are no conflicts to declare.

Acknowledgements

This work is supported by the National Natural Science Foundation of China (grants no. 61805064 and 12104105), the Fundamental Research Funds for the Central Universities of China (grants no. PA2021KCPY0052, JZ2021HGQA0259, and JZ2021HGTA0143), and the Start-up Funding of Guangdong Polytechnic Normal University (grant no. 2021SDKYA033).

References

1 F. Strocchi, *Symmetry Breaking*, Springer-Verlag, Berlin, 2005.

2 L. Kelvin, *Baltimore Lectures on Molecular Dynamics and the Wave Theory of Light*, C. J. Clay and Sons, London, 1904.

3 T. Mori, *Chem. Rev.*, 2021, **121**, 2373.

4 B. Semnani, J. Flannery, R. Al Maruf and M. Bajcsy, *Light: Sci. Appl.*, 2020, **9**, 23.

5 M. Ren, E. Plum, J. Xu and N. I. Zheludev, *Nat. Commun.*, 2012, **3**, 833.

6 A. Lininger, G. Palermo, A. Guglielmelli, G. Nicoletta, M. Goel, M. Hinczewski and G. Strangi, *Adv. Mater.*, 2022, 2107325.

7 H. Liu, D. A. Genov, D. M. Wu, Y. M. Liu, Z. W. Liu, C. Sun, S. Zhu and X. Zhang, *Phys. Rev. B: Condens. Matter Mater. Phys.*, 2007, **76**, 073101.

8 N. Engheta and D. L. Jaggard, *IEEE Antennas Propag. Soc. Newsl.*, 1988, **30**, 6.

9 M. Decker, M. W. Klein, M. Wegener and S. Linden, *Opt. Lett.*, 2007, **32**, 856.

10 M. Qiu, L. Zhang, Z. Tang, W. Jin, C. W. Qiu and D. Y. Lei, *Adv. Funct. Mater.*, 2018, **28**, 1803147.

11 E. Plum and N. I. Zheludev, *Appl. Phys. Lett.*, 2015, **106**, 221901.

12 Z. Wang, H. Jia, K. Yao, W. Cai, H. Chen and Y. Liu, *ACS Photonics*, 2016, **3**, 2096.

13 Z. Tang, *Chiral Nanomaterials: Preparation, Properties and Applications*, John Wiley & Sons, Hoboken, NJ, USA, 2018.

14 Y. Wen, M. Q. He, Y. L. Yu and J. H. Wang, *Adv. Colloid Interface Sci.*, 2021, **289**, 102376.

15 Y. Luo, C. Chi, M. Jiang, R. Li, S. Zu, Y. Li and Z. Fang, *Adv. Opt. Mater.*, 2017, **5**, 1700040.

16 S. Xiao, T. Wang, T. Liu, C. Zhou, X. Jiang and J. Zhang, *J. Phys. D: Appl. Phys.*, 2020, **53**, 503002.

17 V. A. Fedotov, M. Rose, S. L. Prosvirnin, N. Papasimakis and N. I. Zheludev, *Phys. Rev. Lett.*, 2007, **99**, 147401.

18 W. Ma, F. Cheng and Y. Liu, *ACS Nano*, 2018, **12**, 6326.

19 M. Li, L. Guo, J. Dong and H. Yang, *J. Phys. D: Appl. Phys.*, 2014, **47**, 185102.

20 Y. Cheng, H. Chen, J. Zhao, X. Mao and Z. Cheng, *Opt. Mater. Express*, 2018, **8**, 1399.

21 D. B. Stojanović, G. Gligorić, P. P. Beličev, M. R. Belić and L. Hadžievski, *IEEE J. Sel. Top. Quantum Electron.*, 2020, **27**, 4700506.

22 J. Peng, X. He, C. Shi, J. Leng, F. Lin, F. Liu, H. Zhang and W. Shi, *Phys. E*, 2020, **124**, 114309.

23 X. He and W. Cao, *Opt. Mater. Express*, 2023, **13**, 413.

24 V. A. Fedotov, P. L. Mladyonov, S. L. Prosvirnin, A. V. Rogacheva, Y. Chen and N. I. Zheludev, *Phys. Rev. Lett.*, 2006, **97**, 167401.

25 R. Zhang, Q. Zhao, X. Wang, K. M. Lau, T. K. Yung, J. Li and W. Y. Tam, *Nanophotonics*, 2022, **11**, 495.

26 M. V. Gorkunov, A. A. Antonov and Y. S. Kivshar, *Phys. Rev. Lett.*, 2020, **125**, 093903.

27 M. V. Gorkunov, A. A. Antonov, V. R. Tuz, A. S. Kupriianov and Y. S. Kivshar, *Adv. Opt. Mater.*, 2021, **9**, 2100797.

28 L. Ouyang, W. Wang, D. Rosenmann, D. A. Czaplewski, J. Gao and X. Yang, *Opt. Express*, 2018, **26**, 31484.

29 H. Tang, D. Rosenmann, D. A. Czaplewski, X. Yang and J. Gao, *Opt. Express*, 2022, **30**, 20063.

30 B. Tang, Z. Li, E. Palacios, Z. Liu, S. Butun and K. Aydin, *IEEE Photonics Technol. Lett.*, 2017, **29**, 295.

31 W. Li, Z. J. Coppens, L. V. Besteiro, W. Wang, A. O. Govorov and J. Valentine, *Nat. Commun.*, 2015, **6**, 8379.

32 Z. Shen, X. Fang, S. Li, W. Yin, L. Zhang and X. Chen, *Opt. Lett.*, 2022, **47**, 505.

33 Z. Wang, F. Cheng, T. Winsor and Y. Liu, *Nanotechnology*, 2016, **27**, 412001.

34 K. Koshelev, S. Lepeshov, M. Liu, A. Bogdanov and Y. Kivshar, *Phys. Rev. Lett.*, 2018, **121**, 193903.

35 M. Kang, S. Zhang, M. Xiao and H. Xu, *Phys. Rev. Lett.*, 2021, **126**, 117402.

36 J. Jin, X. Yin, L. Ni, M. Soljačić, B. Zhen and C. Peng, *Nature*, 2019, **574**, 501.

37 X. Y. He, F. T. Lin, F. Liu and W. Z. Shi, *Nanophotonics*, 2022, **11**, 4705.

38 R. M. Saadabad, L. Huang and A. E. Miroshnichenko, *Phys. Rev. B*, 2021, **104**, 235405.

39 C. W. Hsu, B. Zhen, J. Lee, S. L. Chua, S. G. Johnson, J. D. Joannopoulos and M. Soljačić, *Nature*, 2013, **499**, 188.

40 A. Kodigala, T. Lepetit, Q. Gu, B. Bahari, Y. Fainman and B. Kanté, *Nature*, 2017, **541**, 196.

41 H. M. Doeleman, F. Monticone, W. den Hollander, A. Alù and A. F. Koenderink, *Nat. Photonics*, 2018, **12**, 397.

42 R. Chai, W. Liu, Z. Li, H. Cheng, J. Tian and S. Chen, *Phys. Rev. B*, 2021, **104**, 075149.

43 Z. Liu, Y. Xu, Y. Lin, J. Xiang, T. Feng, Q. Cao, J. Li, S. Lan and J. Liu, *Phys. Rev. Lett.*, 2019, **123**, 253901.

44 X. Wang, J. Duan, W. Chen, C. Zhou, T. Liu and S. Xiao, *Phys. Rev. B*, 2020, **102**, 155432.

45 S. Yang, C. Hong, Y. Jiang and J. C. Ndukaife, *ACS Photonics*, 2021, **8**, 1961.

46 M. Gandolfi, A. Tognazzi, D. Rocco, C. De Angelis and L. Carletti, *Phys. Rev. A*, 2021, **104**, 023524.

47 D. R. Abujetas, Á. Barreda, F. Moreno, A. Litman, J. M. Geffrin and J. A. Sánchez-Gil, *Laser Photonics Rev.*, 2020, **15**, 2000263.

48 J. Wu, X. Xu, X. Su, S. Zhao, C. Wu, Y. Sun, Y. Li, F. Wu, Z. Guo, H. Jiang and H. Chen, *Phys. Rev. Appl.*, 2021, **16**, 064018.

49 T. Shi, Z. L. Deng, G. Geng, Y. Zeng, G. Hu, A. Overvig, J. Li, C. W. Qiu, A. Alù, Y. S. Kivshar and X. Li, *Nat. Commun.*, 2022, **13**, 4111.

50 X. Yin, J. Jin, M. Soljačić, C. Peng and B. Zhen, *Nature*, 2020, **580**, 467.

51 X. Zhang, Y. Liu, J. Han, Y. Kivshar and Q. Song, *Science*, 2022, **377**, 1215.

52 S. Wan, K. Wang, F. Wang, C. Guan, W. Li, J. Liu, A. Bogdanov, P. A. Belov and J. Shi, *Opt. Lett.*, 2022, **47**, 3291.

53 B. Zhen, C. W. Hsu, L. Lu, A. D. Stone and M. Soljačić, *Phys. Rev. Lett.*, 2014, **113**, 257401.

54 W. Liu, B. Wang, Y. Zhang, J. Wang, M. Zhao, F. Guan, X. Liu, L. Shi and J. Zi, *Phys. Rev. Lett.*, 2019, **123**, 116104.

55 A. Overvig, N. Yu and A. Alù, *Phys. Rev. Lett.*, 2021, **126**, 073001.

56 Y. Chen, W. Chen, X. Kong, D. Wu, J. Chu and C. W. Qiu, *Phys. Rev. Lett.*, 2022, **128**, 146102.

57 J. R. Piper and S. Fan, *ACS Photonics*, 2014, **1**, 347.

58 Y. Liu, A. Chadha, D. Zhao, J. R. Piper, Y. Jia, Y. Shuai, L. Menon, H. Yang, Z. Ma, S. Fan, F. Xia and W. Zhou, *Appl. Phys. Lett.*, 2014, **105**, 181105.

59 J. Wang, A. Chen, Y. W. Zhang, J. P. Zeng, Y. F. Zhang, X. H. Liu, L. Shi and J. Zi, *Phys. Rev. B*, 2019, **100**, 075407.

60 S. Xiao, M. Qin, J. Duan, F. Wu and T. Liu, *Phys. Rev. B*, 2022, **105**, 195440.

61 C. W. Hsu, B. Zhen, A. D. Stone, J. D. Joannopoulos and M. Soljačić, *Nat. Rev. Mater.*, 2016, **1**, 16048.

62 Z. Cao, J. Chen, S. Deng and H. Chen, *Nanoscale*, 2022, **14**, 3849.

63 Z. C. Li, W. W. Liu, H. Cheng, S. Q. Chen and J. G. Tian, *Opt. Lett.*, 2016, **41**, 3142.

64 X. Ma, C. Huang, M. Pu, Y. Wang, Z. Zhao, C. Wang and X. Luo, *Appl. Phys. Lett.*, 2012, **101**, 161901.

65 J. Park, H. Kim and B. Lee, *Opt. Express*, 2008, **16**, 413.

66 H. Li, B. Chen, M. Qin and L. Wang, *Opt. Express*, 2020, **28**, 205.

67 T. Hu, Y. Wang, L. Wu, L. Zhang, Y. Shan, J. Lu, J. Wang, S. Luo, Z. Zhang, L. Liao, S. Wu, X. Shen and Z. Chen, *Appl. Phys. Lett.*, 2017, **110**, 051101.

68 C. Menzel, C. Rockstuhl and F. Lederer, *Phys. Rev. A*, 2010, **82**, 053811.

69 T. Kaelberer, V. A. Fedotov, N. Papasimakis, D. P. Tsai and N. I. Zheludev, *Science*, 2010, **330**, 1510.

70 Y. He, G. Guo, T. Feng, Y. Xu and A. E. Miroshnichenko, *Phys. Rev. B*, 2018, **98**, 161112(R).

71 P. D. Terekhov, V. E. Babicheva, K. V. Baryshnikova, A. S. Shalin, A. Karabchevsky and A. B. Evlyukhin, *Phys. Rev. B*, 2019, **99**, 045424.

72 H. Li, G. Wei, H. Zhou, H. Xiao, M. Qin, S. Xia and F. Wu, *Phys. Rev. B*, 2022, **105**, 165305.

73 W. Suh, Z. Wang and S. Fan, *IEEE J. Quantum Electronics.*, 2004, **40**, 1511.

74 W. Yin, Z. Shen, S. Li, Y. Cui, F. Gao, H. Hao, L. Zhang and X. Chen, *Opt. Express*, 2022, **30**, 32162.

75 H. Li, M. Qin, L. Wang, X. Zhai, R. Ren and J. Hu, *Opt. Express*, 2017, **25**, 31612.

76 G. Yang, S. U. Dev, M. S. Allen, J. W. Allen and H. Harutyunyan, *Nano Lett.*, 2022, **22**, 2001.

77 K. I. Okhlopkov, A. Zilli, A. Tognazzi, D. Rocco, L. Fagiani, E. Mafakheri, M. Bollani, M. Finazzi, M. Celebrano, M. R. Shcherbakov, C. De Angelis and A. A. Fedyanin, *Nano Lett.*, 2021, **21**, 10438.

78 A. A. Popkova, I. M. Antropov, G. I. Tselikov, G. A. Ermolaev, I. Ozerov, R. V. Kirtaev, S. M. Novikov, A. B. Evlyukhin, A. V. Arsenin, V. O. Bessonov, V. S. Volkov and A. A. Fedyanin, *Laser Photonics Rev.*, 2022, **16**, 2100604.